J. Fluid Mech. (2013), *vol.* 736, *pp.* 594–615.
doi:10.1017/jfm.2013.546

Investigation of the mobile granular layer in bedload transport by laminar shearing flows

Pascale Aussillous[1],†, Julien Chauchat[2], Mickael Pailha[3], Marc Médale[1] and Élisabeth Guazzelli[1]

[1]Aix-Marseille Université, CNRS, IUSTI UMR 7343, 13013 Marseille, France
[2]Grenoble-INP/UJF-Grenoble 1/CNRS, LEGI UMR 5519, Grenoble, F-38041, France
[3]Université de Savoie, POLYTECH Annecy-Chambéry, LOCIE - UMR5271, 73376 Le Bourget du Lac, France

(Received 5 July 2013; revised 25 September 2013; accepted 12 October 2013)

The mobile layer of a granular bed composed of spherical particles is experimentally investigated in a laminar rectangular channel flow. Both particle and fluid velocity profiles are obtained using particle image velocimetry for different index-matched combinations of particles and fluid and for a wide range of fluid flow rates above incipient motion. A full three-dimensional investigation of the flow field inside the mobile layer is also provided. These experimental observations are compared to the predictions of a two-phase continuum model having a frictional rheology to describe particle–particle interactions. Different rheological constitutive laws having increasing degrees of sophistication are tested and discussed.

Key words: granular media, particle/fluid flow, sediment transport

1. Introduction

The erosion of granular beds under the action of fluid shearing flows is a problem that has been continually studied and discussed for over a century. This phenomenon is indeed encountered in a wide range of processes of relevance in nature or industry, such as sediment transport in rivers or oceans and slurry transport in the mining and petroleum industries. The interaction of the flow with the erodible bed can give rise to self-formed morphologies such as ripples and dunes. While in most natural occurrences of these patterns the flow is likely to be turbulent, that is not necessarily so, and laminar flows also generate such features. The similarity in observed morphologies seems to reflect analogies in the underlying physics, and thus using laminar flow can be the simplest way in the laboratory to obtain insights into many aspects of sediment transport and morphodynamics (Lajeunesse *et al.* 2010). The present paper focuses on particle transport in the viscous laminar regime and in particular on the mode of particle motion in which particles roll and slide but stay in continuous contact within the bed, a situation usually referred to as bedload transport (see e.g. Van Rijn 1984). The primary objective is to obtain an adequate formalism to relate the sediment flux to the fluid flow, which is a fundamental step in the understanding of the bed evolution and the emergence of bedforms.

† Email address for correspondence: pascale.aussillous@univ-amu.fr

There are two basic avenues to tackle the modelling of sediment transport by viscous shearing flow, one being erosion–deposition models and the other being continuum modelling. The erosion–deposition model is based on mass conservation of the particles in a mobile monolayer and requires knowledge of the deposition and erosion rates (see e.g. Charru, Mouilleron-Arnould & Eiff 2004). Continuum modelling uses mass conservation and momentum balance and the influence of the particles is captured through rheological laws that can be developed from independent experiments. One of the first attempts at this latter type of modelling is due to Bagnold (1956), who used a viscous rheology for the granular stress deduced from rheological measurements of suspensions of neutrally buoyant particles sheared in an annular Couette flow (Bagnold 1954). This continuum approach has been recently rationalised by Ouriemi, Aussillous & Guazzelli (2009) by using a two-phase model framework having a Newtonian rheology for the fluid phase and frictional rheology for the particle phase. While the erosion–deposition model is likely to be appropriate close to incipient particle motion where only one particle layer is mobile, the continuum approach is more realistic at some distance from onset of motion, as the mobile layer can become much larger than one particle diameter.

In the present paper, we address sediment transport in the laminar viscous regime far from the transport threshold. In this regime, which, as mentioned above, has been termed bedload, the grains entrained by the fluid remain permanently in contact in the bed, and thus hydrodynamic, contact and gravity forces must be simultaneously accounted for (see Andreotti *et al.* 2013, chap. 8). The flow involves several granular layers and bears similarity with submarine avalanches forced by the fluid shear stress (Pailha & Pouliquen 2009). Using a continuum approach is thus relevant and two-phase modelling then offers a general framework to study the flow of this dense granular system. The challenge, however, is to find the constitutive laws that account for the rheological behaviour of the dense mobile particulate system. Since the particles mainly interact through contact forces in the bedload, Ouriemi *et al.* (2009) used a frictional rheology for the particle phase. They adopted the simplest Coulomb friction as a first step and showed that this roughly accounted for the observed cubic variation of the particle flux with the bed shear stress in sediment transport experiments in laminar pipe flow. However, the particle flux was inferred indirectly through bed height evolution measurements and not from direct measurement of particle motion inside the moving sediment. Therefore, the frictional rheology could not be accurately tested. To our knowledge only two studies have attempted to investigate inside the mobile granular layer and to gain direct access to the particle flux. Lobkovsky *et al.* (2008) examine individual particle motion using the index-matching technique in a rectangular pipe in laminar flow conditions. These experiments provide flow observation inside the mobile bed, but only one velocity profile and one concentration profile were shown, with a spatial resolution too low to provide meaningful comparison with any predictions (four data points in their figure 2). Mouilleron, Charru & Eiff (2009) used the same index-matching technique to measure the velocity profiles of the fluid and particles inside the mobile granular layer in a viscous Couette flow. Only six profiles were obtained, with a better, but still low, spatial resolution (five to 10 data points in their figure 4). It should also be stressed that, in this Couette geometry, the thickness of the mobile layer is at most two particle diameters and thus the validity of the continuum approach can be questioned. In these two studies, the particle and fluid properties were not varied, which precludes any testing of the scaling law for sediment transport. There is thus a need for accurate measurements inside the mobile granular layer which yield precise comparison with

the prediction of the two-phase modelling and testing of the rheological constitutive laws. The aim of the present work is precisely to produce an extensive set of experimental data that can be compared to different rheological models available in the literature in order to tell which one can best describe sediment transport.

Following previous experiments (Goharzadeh, Khalili & Jørgensen 2005; Lobkovsky *et al.* 2008), we use an index-matching technique to investigate the mobile layer of a granular bed composed of spherical particles in a rectangular channel flow (see § 2). The originality and relevance of the experiments lie in the use of different combinations of particles and fluids, as well as in the joint measurements of the velocity profiles of the particles and the fluid with unprecedented spatial and temporal resolutions for a wide range of fluid flow rates above incipient motion (typically 300 profiles comprising four to 50 data points). The choice of a Poiseuille over a Couette flow is motivated by the fact that the pressure gradient that drives the flow can produce a large particle flux involving a mobile layer much thicker than one particle diameter (up to 25 particle diameters in the present experiment). This justifies the comparison with a continuum model. The experimental observations are thus compared to the predictions of the two-phase modelling of Ouriemi *et al.* (2009) in § 4 and its full three-dimensional numerical implementation, which is described in § 3. We test three types of rheological laws of increasing sophistication: (i) the Coulomb model with constant friction coefficient previously used by Ouriemi *et al.* (2009); (ii) the granular frictional rheology with a shear-rate-dependent friction coefficient, which has been proposed for dense dry granular flows (see e.g. Forterre & Pouliquen 2008) and extended to particles suspended in a fluid (Cassar, Nicolas & Pouliquen 2005); and (iii) a recent rheological model proposed by Boyer, Guazzelli & Pouliquen (2011), which derives from pressure-imposed rheological measurements of dense suspensions of neutrally buoyant spheres and unifies the rheological behaviour of dense suspensions and granular media. We also provide a full three-dimensional investigation of the flow field inside the mobile layer. Conclusions regarding the validity of the different rheological models are drawn in § 5.

2. Experiments

We use an index-matching technique to investigate the mobile granular layer for the sediment transport of spherical particles in a rectangular channel in the viscous laminar regime. The apparatus consists of a horizontal glass tube (of height $H = 6.5$ cm, width $W = 3.5$ cm and length 100 cm) partially filled with particles, as shown in figure 1(*a*). Two index-matched combinations of particles and fluid are used; see table 1. At the outlet from the channel, the fluid is run into a thermostated fluid reservoir, which ensures a constant temperature of 25 °C across the whole flow loop. From this reservoir, it is returned by a gear pump (Ismatec) into the channel. At the inlet, the fluid goes through a packed bed of large spheres, providing a homogeneous and laminar flow. The pump produces a pulseless fluid delivery and consequently a constant fluid flow rate Q_f, which is determined by measuring the volume of fluid collected in a given time.

A given amount of particles is introduced inside the channel, which is then filled by the fluid. Care was taken to fill the tube entrance, leaving an empty buffer space near the outlet using the following steps (see figure 1*c*). (i) The channel is flipped upside-down (meaning that the top is flipped to the bottom). (ii) Then it is tilted at an angle of 43° from the horizontal with the fluid inlet at the bottom. (iii) The channel is set back horizontally and flipped back to its initial position. The duration of each of

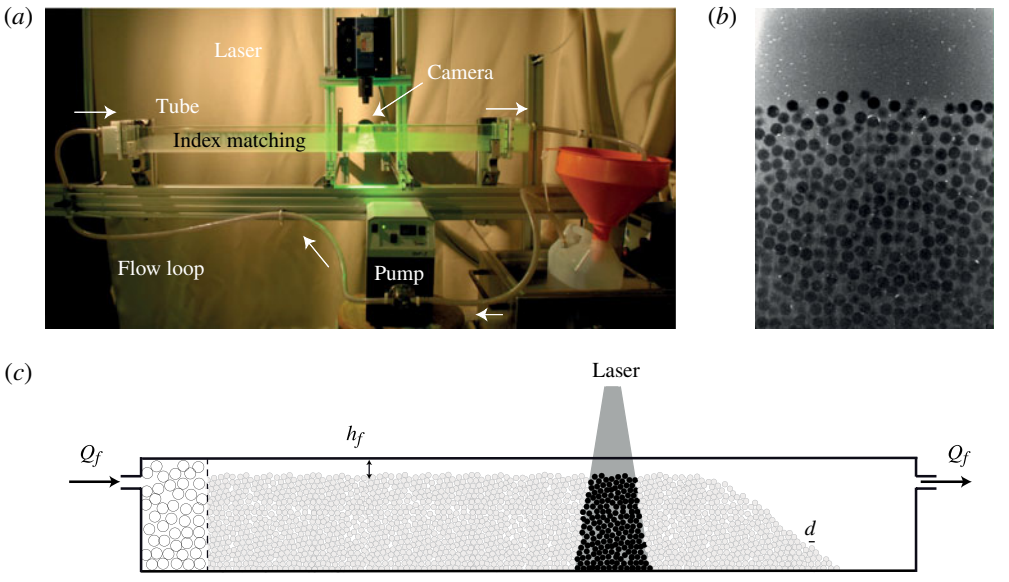

FIGURE 1. (Colour online) (*a*) Experimental apparatus. (*b*) Typical image of the bed test section for run 15: the particles look dark against a brighter fluid and the fluid is seeded with a fluid tracer (a fine fingerprint powder), which appears as white dots (see corresponding supplementary movie 1 available at http://dx.doi.org/10.1017/jfm.2013.546). (*c*) Sketch of the set-up at initial condition.

Combination	A	B
Particles	Borosilicate	PMMA
Fluids	Water (15 wt%) + Triton X-100	Triton X-100
d (mm)	1.1 ± 0.1	2.04 ± 0.03
ρ_p (g cm^{-3})	2.23	1.19
ρ_f (g cm^{-3})	1.06	1.07
η (cP)	320	270
n	1.47	1.49

TABLE 1. Particle and fluid characteristics (at a temperature of 25 °C): particle diameter d, particle density ρ_p, fluid density ρ_f, fluid viscosity η, and refractive index n.

these steps is set to the same sedimentation time (2 and 4 min for combinations A and B, respectively). This procedure fills the tube entrance, leaving an empty buffer space near the outlet. (iv) A small flow rate is applied for typically 4 min to create a small uniform gap (typically five grain diameters) devoid of particles at the top. These four steps are repeated to create a reproducible initial condition for all runs corresponding to a loose bed. After the preparation phase, a given flow rate is imposed and kept constant for the duration of each run (typically 3–5 min). Eroded grains fall out into the empty buffer space at the outlet, leaving an upstream region exhibiting a flat fluid–particle interface, which decreases with time. The characteristics of the different runs performed are summarized in table 2.

Run	Combin.	Q (m^3 s^{-1})	Symbol
1	A	2.7×10^{-6}	× (dark grey; blue online)
2	A	3.6×10^{-6}	○ (dark grey; blue online)
3	A	4.4×10^{-6}	▲ (dark grey; blue online)
4	A	5.3×10^{-6}	□ (dark grey; blue online)
5*	A	5.7×10^{-6}	♦ (dark grey; blue online)
6	A	6.1×10^{-6}	▽ (dark grey; blue online)
7	A	6.9×10^{-6}	• (dark grey; blue online)
8	A	8.2×10^{-6}	△ (dark grey; blue online)
9	A	8.6×10^{-6}	■ (dark grey; blue online)
10	A	9.7×10^{-6}	◊ (dark grey; blue online)
11	B	2.2×10^{-6}	× (mid grey; red online)
12	B	2.7×10^{-6}	○ (mid grey; red online)
13	B	3.2×10^{-6}	▲ (mid grey; red online)
14	B	3.6×10^{-6}	□ (mid grey; red online)
15*	B	4.1×10^{-6}	♦ (mid grey; red online)
16	B	4.6×10^{-6}	▽ (mid grey; red online)
17	B	5.6×10^{-6}	• (mid grey; red online)

TABLE 2. Performed runs. The laser sheet is located at the middle of the tube (17.5 mm from the front wall), except for runs 5 and 15 (denoted by *), where seven runs where performed at different locations: 2.5 mm (×), 5 mm (○), 7.5 mm (▲), 10 mm (□), 12.5 mm (♦), 15 mm (▽) and 17.5 mm (•) from the front wall.

The test section is 4 cm wide to permit good resolution of the particle imaging. It is located at a distance ≈50 cm from the entrance of the tube to avoid end effects and to provide a fully developed laminar flow (Lobkovsky *et al.* 2008). It is illuminated by a green laser sheet (Laser 2000, 532 nm, 100 mW) aligned with the tube length in its middle for most of the experiments; see figure 1(*a*). Successive scans are also performed to obtain a three-dimensional investigation of the flow (runs 5 and 15 indicated in table 2). A digital camera (Basler Scout) with a resolution of 1392×1040 pixels records a sequence of images at a rate of 20 frames per second. A dye (Rhodamine 6G) that fluoresces when illuminated by the laser in the wavelength range greater than 555 nm is added to the fluid. Owing to a red filter (with wavelength bandwidth 590–1800 nm) placed in front of the camera lens, the particles look dark against a brighter fluid, as seen in figure 1(*b*).

The fluid height h_f above the granular layer is measured every 5 s by averaging 10 images (corresponding to averaging over 0.5 s) and detecting the interface between the fluid and the granular layer by the change of slope in the averaged grey-level profile of the obtained averaged image (see figure 2*a*). The error bar is estimated to be half a grain diameter. A typical temporal evolution of h_f is shown in figure 2(*b*). The initially prepared loose bed first experiences a dilation, which reorganizes the entire bed. We may thus assume that the initial preparation plays a role only in this transient dilation regime. The particles are then eroded out of the test section, which induces an increase of h_f (for times $t \gtrsim 30$ s in figure 2*b*). This process slows down with time and eventually stops at a final fluid height (Ouriemi *et al.* 2007; Lobkovsky *et al.* 2008). We do not wait long enough to observe the cessation of particle erosion, which is reached after typically one hour. The runs are stopped when the thickness of the mobile layer corresponds to $\approx d$. Assuming that the flow is steady after the transient dilatation, the flow properties can be determined at each given h_f.

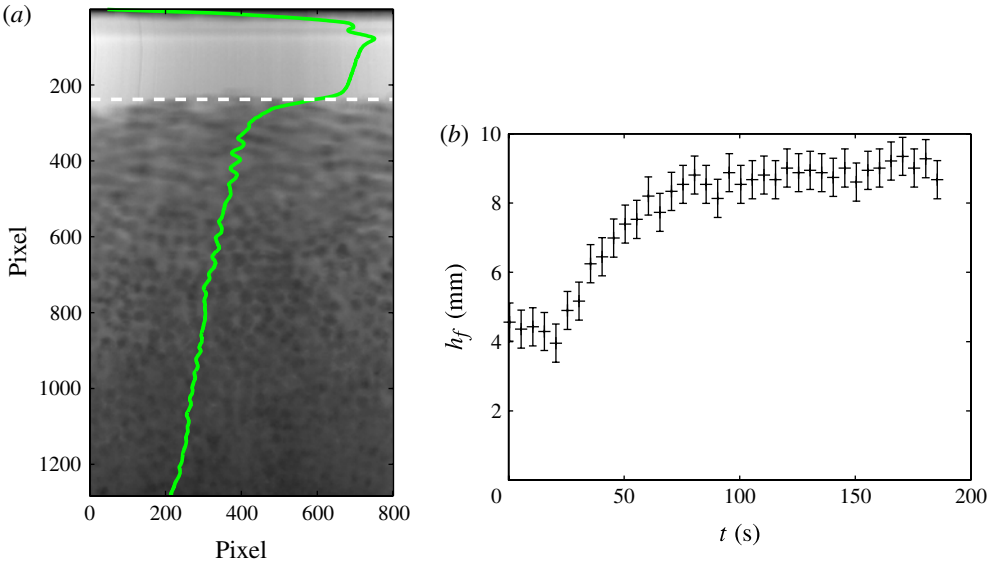

FIGURE 2. (Colour online) (*a*) Averaged image after 35.5 s for run 2 with the corresponding averaged grey-level profile (grey full line; green online) and detected fluid–bed interface (white dashed line). (*b*) Temporal evolution of the fluid height h_f for the same run.

Particle velocities are measured by particle image velocimetry (PIV) using the MATLAB PIV software DPIVsoft (Meunier & Leweke 2003). For a given h_f, 10 pairs of successive images are processed to find the velocity profile, corresponding to an increment from 1 (0.05 s) to 10 (0.5 s) images. In practice, this involves using a square interrogation region having a size $S_{ir} = 64$ pixels ($\approx 2d$), with 45 boxes in the horizontal direction and 60 boxes in the vertical direction. The local particle displacement at each node for each pair is measured using a cross-correlation. The vertical velocity profile is built up by taking the median of the velocity for the 45 horizontal boxes for the 10 pairs of images, excluding displacements below 1 pixel and above $S_{ir}/3$ pixels (see Meunier & Leweke 2003). The error is given by one standard error. The spatial resolution of the measurement (given by the height of the interrogation region) is $\approx 2d$ while the velocity resolution (given by the choice of the image pairs) ranges between 0.06 and 20 mm s^{-1}. In the case of combination B, the fluid is seeded with a fine fingerprint powder (Lightning Powder Company Inc.) used as a fluid tracer; see the white dots in figure 1(*b*). This means that the PIV measurements provide the fluid velocity in the pure fluid phase and a composite velocity between that of the grains and that of the fluid in the granular layer, which is determined by the amount of fingerprint powder in this layer. Since this amount is very small, the PIV measurements mainly give the particle velocity. To determine the full fluid velocity profile, the images are thresholded to capture only the fingerprint powder motion and the same PIV technique is used. However, owing to some loss of tracers during the thresholding process, the velocity profile is less fully resolved and presents larger error bars.

The grey-level intensity gradient (see figure 2*a*) is mainly due to two effects (Dijksman *et al.* 2012): (i) linear broadening of the laser line due to the use of a laser line generator with a finite fan angle; and (ii) absorption due to the presence of the dye leading to an exponential decrease in intensity. Assuming that the second

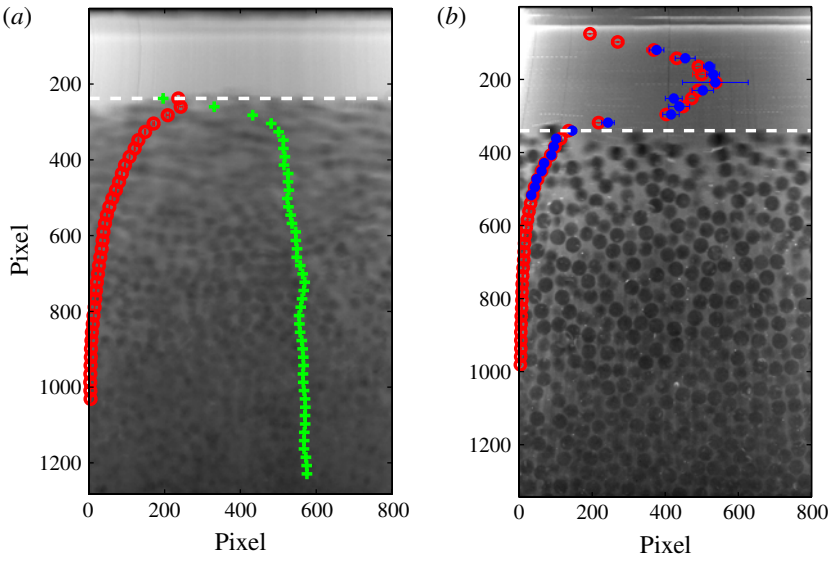

FIGURE 3. (Colour online) Averaged images with the corresponding particle plus fluid tracer (fingerprint powder) (∘; red online) and solely fluid tracer (∗; blue online) velocity profiles and particle volume fraction (+; green online) for two runs. (*a*) Run 2 (combination A) after 35.5 s: velocity scale $= 0.025$ mm s^{-1} pixel^{-1}, length scale $= 0.029$ mm pixel^{-1}, particle volume fraction scale $= 0.001$ pixel^{-1}; see corresponding supplementary movie 2. (*b*) Run 16 (combination B for which the fluid is seeded) after 115.5 s: velocity scale $=$ 0.025 mm s^{-1} pixel^{-1}, length scale $= 0.046$ mm pixel^{-1}; see corresponding supplementary movie 3. The white horizontal dashed line indicates the fluid–particle interface.

effect remains negligible in our experiment, the particle volume fraction is estimated by using the averaged grey-level profile of the 10 images (averaged on the same box size as in the PIV) and scaling it by the grey-level profile of the immobile initial bed, which is assumed to be at a constant particle volume fraction of 0.585. The particle volume fraction can be estimated for combination A but not for combination B because of a poorer contrast.

From these measurements, we obtain approximately 300 particle concentration and velocity profiles at (approximately 10–40 depending on the run duration/flow rate) different fluid heights for the 17 different runs, which range over a large extent of flow rates and correspond to two different combinations of particles and fluid (see table 2). The data are available as supplementary material (available at http://dx.doi.org/10.1017/jfm.2013.546) in a text file and a MATLAB file. Typical particle volume fraction and velocity profiles for the two combinations A and B of particles and fluid are shown in figure 3. The background image corresponds to averaging the 10 images used in the PIV. Two important observations that are in accordance with the previous findings of Lobkovsky *et al.* (2008) and Mouilleron *et al.* (2009) can be made. (i) There is no velocity slip between the particles and the fluid inside the mobile granular layer. (ii) The particle volume fraction is approximately constant inside this layer except at the top interface where it vanishes on a distance $\approx 2d$. From the velocity and concentration profiles, we can deduce the particle flux q_p and the thickness h_m of the mobile layer. Since the concentration profile is not precisely resolved, it is more convenient to measure the particle velocity flux q_v, which is simply given by integrating the particle velocity profile. Note that this q_v corresponds

to a two-dimensional particle velocity flux measured in a vertical plane (in the middle vertical plane of the channel for most of the experiments). The thickness h_m of the mobile layer is obtained by finding the position inside the layer where a cut-off velocity having a value of 0.09 mm s^{-1} is reached. The uncertainty on q_v is given by the sum of the velocity uncertainties and that on h_m is estimated to be $d/2$.

We also need to determine the two-dimensional fluid flow rate q_f from the evaluation of the three-dimensional fluid flow rate Q_f. The switch to a two-dimensional flow rate is given by $q_f = kQ_f/W$ with a geometrical coefficient k, which only depends on the aspect ratio h_f/W and the lateral position from the centre y/W:

$$k = \frac{W}{h_f} \frac{1 - \dfrac{96}{\pi^4} \displaystyle\sum_{n=0}^{\infty} \frac{\cosh[(2n+1)\pi y/W]}{(2n+1)^4 \cosh[(n+\frac{1}{2})\pi W/h_f]}}{\dfrac{W}{h_f} - \dfrac{192}{\pi^5} \displaystyle\sum_{n=0}^{\infty} \frac{\tanh[(n+\frac{1}{2})\pi W/h_f]}{(2n+1)^5}}. \tag{2.1}$$

The calculation derived from Nicolas, Luijkx & Platten (2000) that leads to (2.1) assumes a solid bed surface (meaning also no-slip boundary condition) and thus expression (2.1) is likely to be valid at relatively small flow rate for which the perturbation induced onto the Poiseuille flow by the motion of the granular medium is negligible. In the centre of the channel this coefficient k varies from 1.12 to 1.35 in the range of fluid height h_f explored in the experiments.

Another important dimensionless number of the problem that controls incipient motion is the Shields number θ. It is basically the shear stress at the top of the bed scaled by the hydrostatic pressure difference across a particle. To infer this number, we follow the same approach as above (Ouriemi *et al.* 2007). It is given by $\theta = 6k(Re/Ga)(d/h_f)^2$, where the Reynolds number $Re = \rho_f Q_f/(\eta W)$ and the Galileo number $Ga = \rho_f(\rho_p - \rho_f)gd^3/\eta^2$. In the present experiments performed in the viscous laminar regime, both θ and Re range from 0.2 to 1.2.

3. Two-phase modelling

3.1. *Governing equations*

We use the classical two-phase equations (see e.g. Jackson 1997, 2000) with closures proposed by Ouriemi *et al.* (2009) as appropriate to the present bed erosion problem. We consider a flat particle bed of thickness h_p submitted to a Poiseuille flow driven by a pressure gradient $\partial p^f/\partial x$ in a horizontal channel. For simplicity we focus first on the two-dimensional situation (see figure 4*a*) and the flow is taken as stationary, uniform and parallel. The velocities thus reduce to their components along the horizontal x-direction and are designated as u^f for the fluid velocity, u^p for the particle velocity and $U = \phi u^p + (1-\phi)u^f$ for the volume average velocity, where ϕ is the particle volume fraction. The three-dimensional implementation of the two-phase model is discussed in § 3.3.

The two-phase equations can be written by considering either the two phases (fluid and particles) or one phase (fluid or particles) and the bulk suspension. Considering bulk and fluid phase equations proves to be more convenient as we limit consideration to viscous flow of a granular bed. Along the horizontal x-direction, the fluid phase equation reduces to the Brinkman equation (see Brinkman 1947) for the fluid velocity,

$$\frac{\partial p^f}{\partial x} - \frac{\partial \tau^f}{\partial z} + \frac{\eta}{K}(U - u^p) = 0 \tag{3.1}$$

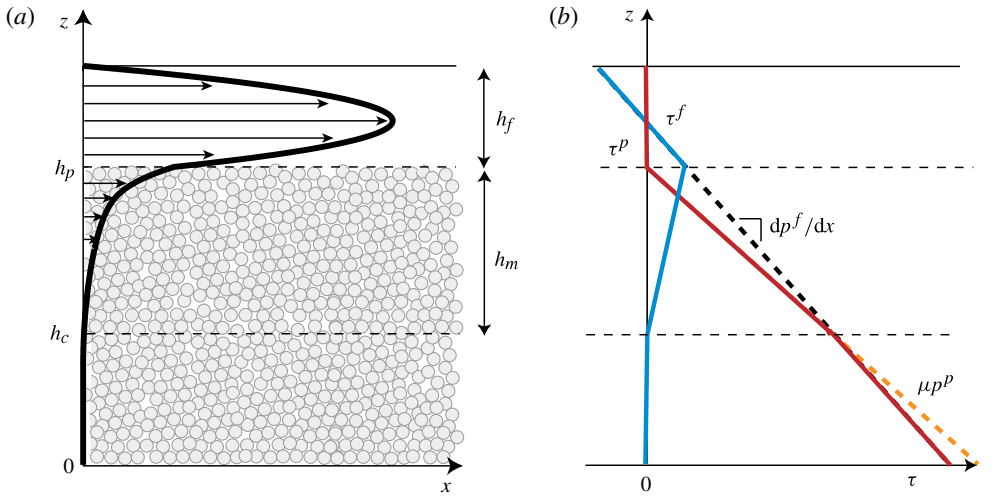

FIGURE 4. (Colour online) Sketches of (*a*) the particle bed submitted to a Poiseuille flow and (*b*) the exchange between the fluid τ^f (mid grey; blue online) and particle τ^p (slightly darker grey; red online) stresses inside the granular bed.

and the momentum equation for the mixture (particles plus fluid) is written as

$$\tau^p(z) + \tau^f(z) = \tau^f(h_p) - \frac{\partial p^f}{\partial x}(h_p - z), \tag{3.2}$$

when integrated from the bed interface position h_p to an arbitrary vertical position z inside the sediment. The Brinkman equation (3.1) describes in particular the fluid flow through the granular bed. The shear stress of the particle phase is denoted τ^p and the interphase force is the dominant viscous Darcy drag, with η the fluid viscosity and K the permeability given by the Carman equation $K = (1-\phi)^3 d^2/180\phi^2$ with d the particle diameter (see e.g. Goharzadeh *et al.* 2005; Van der Hoef, Beetstra & Kuipers 2005). The mixture equation (3.2) accounts for the transfer between the fluid stress at the top of the bed and the stresses of the fluid (τ^f) and solid (τ^p) phases inside the bed. The momentum equations along the vertical z-direction show that the pressure of the fluid phase along gravity is simply the hydrostatic pressure and that the pressure of the particle phase is proportional to the apparent weight of the solid phase and increases when penetrating inside the bed,

$$p^p = \phi \Delta\rho g(h_p - z), \tag{3.3}$$

where $\Delta\rho = \rho_p - \rho_f$ corresponds to the density difference between the two phases.

3.2. *Closures*

To close (3.1) and (3.2), we follow Ouriemi *et al.* (2009) and consider that the stress tensor of the fluid phase is of Newtonian form $\tau^f(z) = \eta_e(\mathrm{d}U/\mathrm{d}z)$ with an effective viscosity η_e, while that of the particle phase comes only from direct particle–particle interactions and is described by a frictional rheology in the mobile granular layer ($\mathrm{d}u^p/\mathrm{d}z > 0$) for which $\tau^p = \mu p^p$ with a friction coefficient μ. We have tested three types of constitutive laws of increasing sophistication.

(i) A Coulomb model with constant friction coefficient ($\mu = \mu_s$, the tangent of the angle of repose) combined with an Einstein effective viscosity $\eta_e = \eta(1 + 5\phi/2)$,

where the volume fraction is considered constant and ≈0.55 inside the granular layer, i.e. $\eta_e/\eta \approx 2.4$. Note that it may be surprising to use the Einstein viscosity, which is supposed to be valid for dilute suspensions, while, in the present experimental configuration, the particles are in contact and thus the volume fraction is not far from close packing. However, as the particles are mainly in contact, higher-order hydrodynamic interactions such as lubrication may be disregarded (Ouriemi *et al.* 2009). The situation is similar to that of a porous medium for which the viscosity is commonly taken as close to the Einstein viscosity (see e.g. Goharzadeh *et al.* 2005).

(ii) A granular frictional rheology, which has been proposed for dense dry granular flows (see e.g. Forterre & Pouliquen 2008) and extended to particles suspended in a fluid (Cassar *et al.* 2005) with a shear-rate-dependent friction coefficient $\mu(I) = \mu_1 + I(\mu_2 - \mu_1)/(I + I_0)$ where I is a dimensionless shear rate that corresponds to the ratio between the time of rearrangement of a particle when it is displaced from its hole and the time taken by the particle to move from one hole to the next (I_0, μ_1 and μ_2 are constants that depend upon the particle material and shape used). While for dry granular flows the particulate system is governed by an inertial number $I = d\dot{\gamma}^p\sqrt{\rho_p/p^p}$, it is governed by a viscous number $I_v = \eta\dot{\gamma}^p/p^p$ where $\dot{\gamma}^p$ is the particle shear rate for wet granular flows. For simplicity, the particle volume fraction ϕ and the effective viscosity η_e are again kept constant.

(iii) A suspension rheology with a friction $\mu(I_v)$ with $\mu_1 = 0.32$, $\mu_2 = 0.7$ and $I_0 = 0.005$, which is supplemented by a shear-rate-dependent volume fraction constitutive law $\phi(I_v) = \phi_m/(1 + I_v^{1/2})$ and by an effective viscosity $\eta_e(\phi) = \eta[1 + \frac{5}{2}\phi(1 - \phi/\phi_m)^{-1}]$, which diverges at maximum volume fraction $\phi_m = 0.585$. This constitutive model has been recently proposed by Boyer *et al.* (2011) and comes from rheological measurements of dense suspensions of neutrally buoyant spheres using pressure-imposed rheometry.

3.3. *Implementation*

The two-dimensional calculation can be conducted analytically for the simplest Coulomb model (case (i) of § 3.2). It is presented with some details here as it gives physical insights into the mechanisms involved as well as the appropriate scalings. There are three key simplifications that permit the calculation to be tackled analytically. First, the friction coefficient, μ, is a constant. Second, the volume fraction ϕ is considered constant inside the granular bed and thus the effective viscosity η_e is also a constant. Third, the Darcy drag term is dominant in the Brinkman equation (3.1). Therefore, inside the bed, there is very little slip between the two phases and both particle and fluid phases move at the velocity of the mixture, $u^f = u^p = U$. This last assumption is important because the problem is then reduced to simply solving the mixture equation (3.2).

The mixture equation (3.2) shows that the mixture shear stress $\tau^f + \tau^p$ increases linearly with depth from the surface value $\tau^f(h_p)$ due to the horizontal pressure gradient $\partial p^f/\partial x$. The shear stress of the particle phase is the (constant) friction coefficient, μ, multiplied by the particle pressure given by (3.3), i.e. $\tau^p = \mu p^p = \mu\phi\Delta\rho g(h_p - z)$, while that of the fluid phase is $\tau^f = \eta_e\,\mathrm{d}U/\mathrm{d}z$. Therefore the mixture equation (3.2) can be rewritten as

$$\mu\phi\Delta\rho g(h_p - z) + \eta_e\frac{\mathrm{d}U}{\mathrm{d}z} = \tau^f(h_p) - \frac{\partial p^f}{\partial x}(h_p - z), \tag{3.4}$$

with zero shear at $z = h_c$, zero particle shear stress at $z = h_p$, and no-slip conditions on the channel boundaries.

Equation (3.4) describes the exchange between the shear stress of the fluid phase τ^f and that of the solid phase τ^p (see figure 4*b*). On the one hand, the shear stress of the fluid phase $\tau^f = \eta_e \, \mathrm{d}U/\mathrm{d}z = \tau^f(h_p) - (\mu\phi\Delta\rho g + \partial p^f/\partial x)(h_p - z)$ is equal to $\tau^f(h_p)$ at the top of the granular bed, at $z = h_p$, and goes to zero at the bottom of the mobile layer, at $z = h_c$, given by $h_p - h_c = \tau^f(h_p)/(\mu\phi\Delta\rho g + \partial p^f/\partial x)$. On the other hand, the shear stress of the particle phase is zero at $z = h_p$ and increases inside the bed since $\tau^p = \mu p^p = \mu\phi\Delta\rho g(h_p - z)$. The particle shear stress can keep the value μp^p until it reaches $z = h_c$ for which granular motion stops.

Equation (3.4) can be solved analytically for this simple Coulomb model to infer the thickness of the mobile granular layer $h_m = h_p - h_c$ and the velocity profile. The thickness of the mobile granular layer is given by

$$\frac{h_m}{h_f} = \frac{\eta_e}{\eta}\left[\sqrt{1 - \frac{\eta}{\eta_e}\frac{\partial p^f/\partial x}{\partial p^f/\partial x + \mu\phi\Delta\rho g}} - 1\right], \tag{3.5}$$

where h_f is the fluid height. This result provides immediate clues about the relevant scalings of the problem. The length scale is given by the fluid height h_f, the pressure scale by the hydrostatic pressure $\Delta\rho g h_f$, and thus the time scale by $\eta/\Delta\rho g h_f$ (as suggested by the definition of the viscous number $I_v = \eta\dot{\gamma}^p/p^p$). This relation (3.5) was previously found by Ouriemi *et al.* (2009) (see their table 4) but in this work the length was made dimensionless by the height of the channel and not by that of the fluid. It should be stressed that these scalings are not restricted to the present Poiseuille problem but also apply for example to a particle bed submitted to a Couette flow; see table 8 of Ouriemi *et al.* (2009).

Inside the bed ($z \leqslant h_p$), the velocity profile is

$$u^p = u^f = U = \frac{\partial p^f/\partial x + \mu\phi\Delta\rho g}{\eta_e}\frac{(z - h_c)^2}{2}, \tag{3.6}$$

and is parabolic. It can also be calculated in the pure fluid region ($h_p \leqslant z \leqslant h_p + h_f$) and reads

$$u^f = U = \frac{1}{\eta}\frac{\partial p^f}{\partial x}\frac{(z - h_p - h_f)(z - h_p)}{2} + U(h_p)\frac{(h_p + h_f - z)}{h_f}. \tag{3.7}$$

Integration of these velocity profiles gives the granular and fluid flow rates,

$$q_p = \frac{\Delta\rho g h_f^3}{\eta}\left[\frac{\phi}{6}\frac{\eta}{\eta_e}\left(\frac{h_m}{h_f}\right)^3\left(\frac{\partial p^f/\partial x}{\Delta\rho g} + \mu\phi\right)\right] \tag{3.8}$$

and

$$q_f = \frac{\Delta\rho g h_f^3}{\eta}\left\{-\frac{1}{12}\frac{\partial p^f/\partial x}{\Delta\rho g} + \frac{\eta}{\eta_e}\left(\frac{\partial p^f/\partial x}{\Delta\rho g} + \mu\phi\right)\left[\frac{1}{4}\left(\frac{h_m}{h_f}\right)^2 + \frac{1-\phi}{6}\left(\frac{h_m}{h_f}\right)^3\right]\right\}, \tag{3.9}$$

respectively. The relevant scaling for the flow rate is thus $\Delta\rho g h_f^3/\eta$. It clearly does not involve the particle diameter as expected from the present continuum modelling. This calculation also shows that the control parameter is the dimensionless fluid flow rate.

For the more complex granular and suspension rheologies, equation (3.4), which is now nonlinear through the constitutive laws for $\mu(I_v)$, $\phi(I_v)$ and $\eta_e(\phi)$, can be solved numerically using MATLAB. It is important to mention that the only assumption that we keep is that the Darcy drag term is dominant in the Brinkman equation (3.1) and that the problem is therefore reduced to simply solving the mixture equation (3.2). This important simplification is supported by the experimental evidence that there is very little slip between the two phases (see § 2). The full three-dimensional implementation of the original mixture equations has been undertaken in an in-house finite element research code, in which the frictional granular rheology is handled using a regularization technique (Chauchat & Médale 2010, 2013). In this latter numerical model, the fluid–bed interface is fixed and no-slip boundary conditions are imposed on the walls for the mixture.

4. Comparison

First, we present the experimental data (taken in the middle plane of the rectangular channel) for q_v and h_m, respectively, versus fluid height h_f in figure 5(*a*,*b*) and discuss the appropriate scalings in figure 5(*c*,*d*). Clearly, for a given run, q_v and h_m present a decrease with increasing h_f. This can be understood as follows using figure 4(*a*,*b*). With increasing time, the bed is eroded and the fluid thickness h_f increases. Since the flow rate is constant, this leads to a decrease in fluid stress gradient and consequently a decrease in thickness of the mobile layer h_m (see figure 4*b*). The particle velocity flux q_v is a growing function of h_m (see (3.8)). Therefore it also decreases with increasing h_f. For the same reason, q_v and h_m increase with the flow rate for a given particle and fluid combination. Finally, the combination B (PMMA particles) leads to higher q_v and h_m than combination A (borosilicate particles). This is due to the fact that a lower pressure gradient of the particle phase is obtained with combination B (see (3.3)). This gives a lower particle stress gradient ($\tau^p = \mu p^p$); see again figure 4(*b*). A good collapse is obtained in figure 5(*c*,*d*) when using the scalings coming from the continuum approach described in § 3 (the error bars are calculated using the rules for error propagation). This suggests that this approach contains a good physical ingredient, i.e. a frictional rheology of the mobile granular layer. Moreover, the dimensionless fluid flow rate $q_f/(\Delta\rho g h_f^3/\eta)$ is a good control parameter, and h_f and $\eta/\Delta\rho g h_f$ can be taken as the length scale and time scale, respectively. These scalings are used in the following. An alternative scaling commonly found in the literature is to use the particle diameter d as the length scale and the Shields number as the control parameter; see figure 5(*e*,*f*). The collapse of the data presents slightly larger scatters but this can still be seen as appropriate.

We now turn to a quantitative comparison with the two-phase modelling using the (i) Coulomb and (ii) granular rheologies in figure 6. We have also selected typical velocity profiles corresponding to different runs for the two combinations A and B (see table 2) at three different dimensionless flow rates in figure 7. The good collapse of the different profiles for each dimensionless flow rate shows again that the scalings given by the continuum modelling of § 3 are relevant.

The Coulomb rheology using a realistic $\mu_s = 0.32$ (Boyer *et al.* 2011) and an Einstein effective viscosity $\eta_e/\eta = 2.4$ yields sensible q_v but fails in predicting h_m (see the grey (magenta online) dashed-dotted lines in figure 6). This discrepancy can be evidenced on the velocity profiles of figure 7. The predicted flow inside the mobile layer gives larger velocity at the fluid–bed interface and smaller thickness of the mobile layer (see the grey (magenta online) dashed-dotted lines in figure 7(*b*,*d*,*f*).

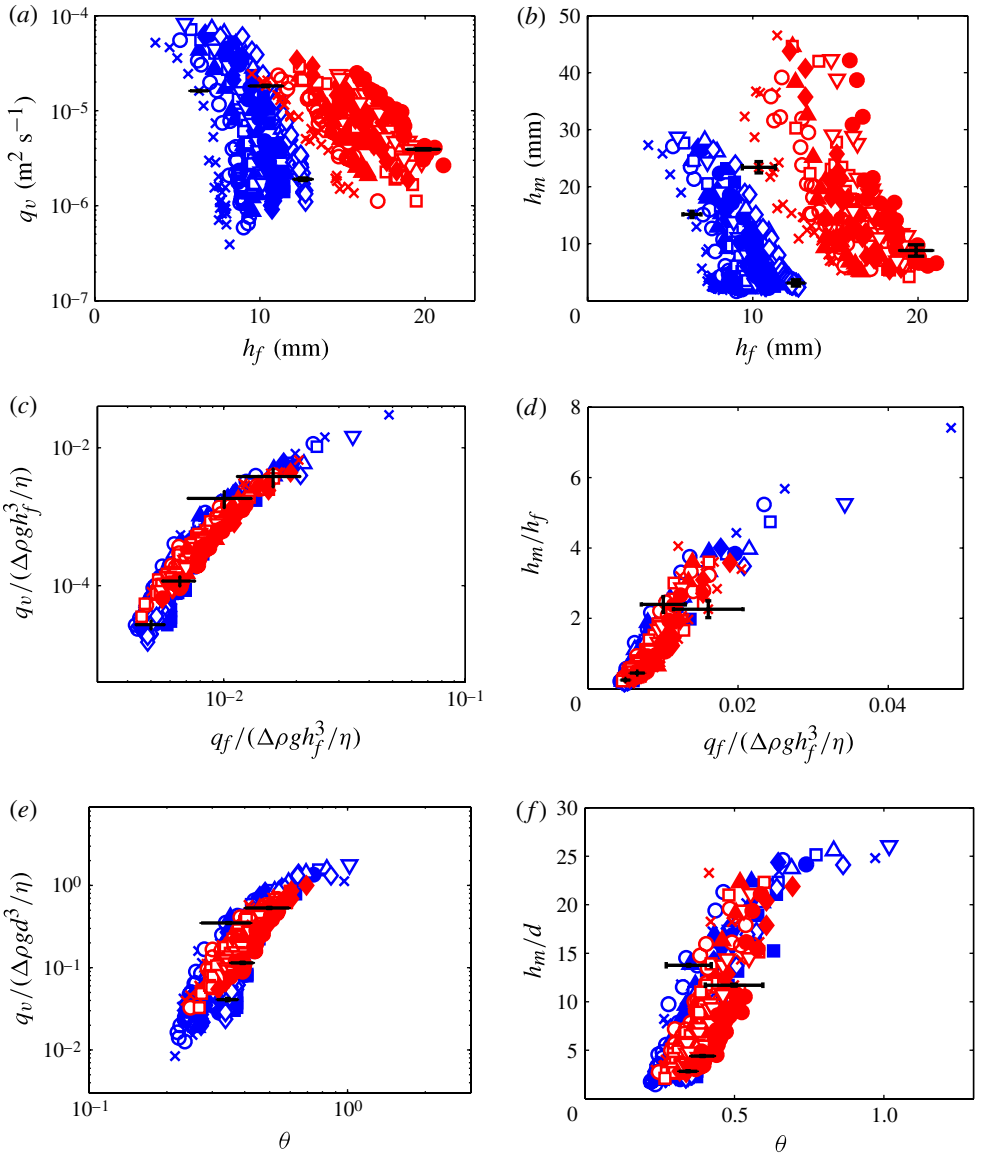

FIGURE 5. (Colour online) (*a*) Experimental particle velocity flux q_v and (*b*) thickness of the mobile layer h_m versus fluid height h_f for the different runs listed in table 2 for the different combinations A (dark grey symbols; blue online) and B (mid grey symbols; red online). (*c*) Particle velocity flux q_v made dimensionless by $\Delta\rho g h_f^3/\eta$ and (*d*) thickness of the mobile layer made dimensionless by h_f versus fluid flow rate q_f made dimensionless by $\Delta\rho g h_f^3/\eta$. (*e*) Particle velocity flux q_v made dimensionless by $\Delta\rho g d^3/\eta$ and (*f*) thickness of the mobile layer h_m made dimensionless by d versus Shields number θ. For clarity, only two error bars (in black) for the most extreme values have been shown for each combination.

These two effects compensate each other to give reasonable predictions for q_v, but neither the velocity profile nor the thickness of the mobile layer h_m are correctly described.

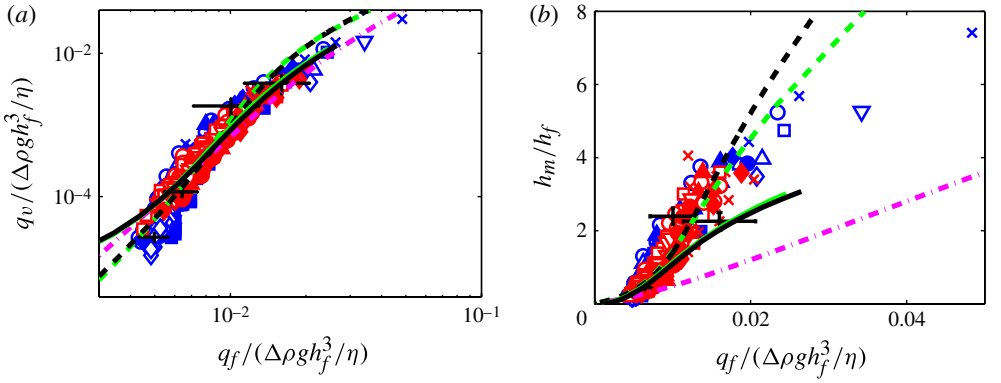

FIGURE 6. (Colour online) Dimensionless (*a*) particle velocity flux $q_v/(\Delta\rho g h_f^3/\eta)$ and (*b*) thickness of the mobile layer h_m/h_f versus dimensionless flow rate $q_f/(\Delta\rho g h_f^3/\eta)$ compared to the two-phase model using (i) the Coulomb rheology with $\mu_s = 0.32$ and $\eta_e/\eta = 2.4$ (dark grey dashed-dotted line; magenta online) and with $\mu_s = 0.24$ and $\eta_e/\eta = 14$ (2D, light grey dashed line (green online); and 3D, light grey solid line (green online), for $h_f = 8$ mm) and (ii) the granular rheology with $\mu_1 = 0.24$, $\mu_2 = 0.39$, $I_0 = 0.01$ and $\eta_e/\eta_f = 6.6$ (2D, black dashed line; and 3D, black solid line, for $h_f = 8$ mm). The symbols correspond to the different runs for the two different combinations listed in table 2. As in figure 5, only two error bars (in black) have been shown for each combination.

Instead of using the above commonly used values for μ_s and η_e/η, the method of least squares can be used to fit the data for q_v and h_m, as well as the interface velocity, and leads to a better agreement for a smaller $\mu_s = 0.24$ and a larger $\eta_e/\eta = 14$ (see the light grey (green online) dashed lines in figure 6). Good agreement is also found for the velocity profiles at small flow rates (see the light grey (green online) dashed lines in figure 7*a–d*). At large flow rates, this model gives a good prediction in the fluid region but leads to a large overestimation in the mobile granular layer (see the light grey (green online) dashed lines in figure 7*e*,*f*). This overestimation can also be seen in figure 6 above a dimensionless flow rate of $\approx 10^{-2}$, for which the bedload thickness is of the order of the channel size.

Obviously, three-dimensional effects must be taken into account, as seen by the better agreement with the three-dimensional numerical simulations for q_v at large flow rate (see the light grey (green online) solid line in figure 6*a*). Note that there is some discrepancy at small flow rates due to numerical problems linked to the regularization technique. The thickness of the mobile layer h_m is also underestimated at large flow rate (see the light grey (green online) solid line in figure 6*b*). Nonetheless, the three-dimensional simulations lead to a saturation of h_m, which is consistent with the experimental data, whereas the two-dimensional calculations show a continuous increase. Note that the poor quantitative agreement obtained for h_m is also due to the great difficulty in determining accurately $\dot{\gamma}^p = 0$ on the velocity profiles both in the experiments and in the computations. Similar behaviour can be seen in the velocity profiles of figure 7. At relatively small flow rate (see figure 7*a–d*) both two- and three-dimensional predictions are superimposed and are in good agreement with the experimental data. At larger flow rate (see figure 7*e*,*f*) the two-dimensional model provides good predictions in the fluid region but yields an overestimation in the mobile granular layer, whereas the three-dimensional model gives a better prediction inside the mobile layer and a slight overestimation in the pure fluid region.

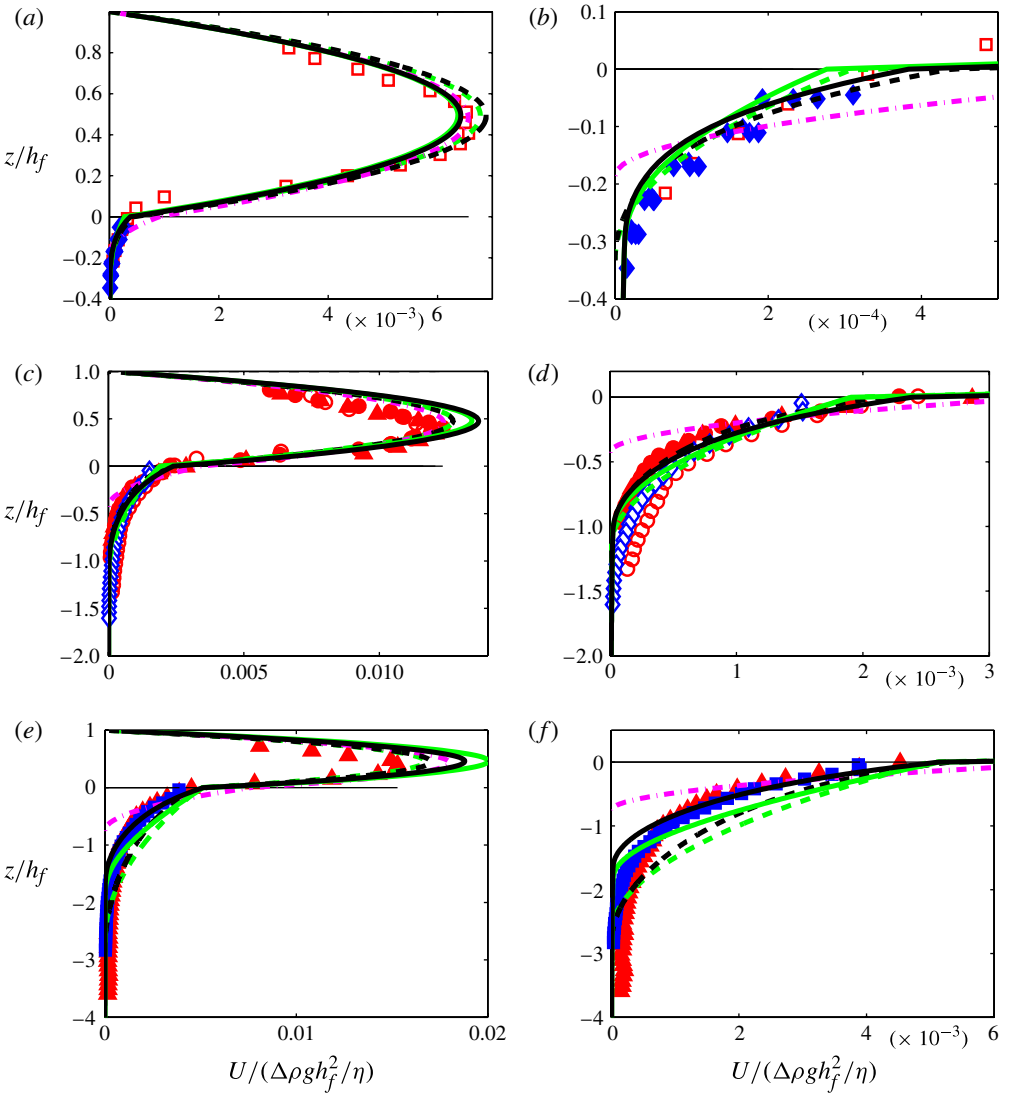

FIGURE 7. (Colour online) Comparison of the dimensionless experimental (symbols corresponding to the runs in table 2) and theoretical (same line representations as in figure 7) velocity profiles for three dimensionless flow rates: (*a*) $q_f/(\Delta\rho g h_f^3/\eta) = 4.6\times10^{-3}$, (*c*) 9.1×10^{-3} and (*e*) 13.9×10^{-3}. Graphs (*b*), (*d*) and (*f*) are blow-ups of graphs (*a*), (*c*) and (*e*), respectively.

Comparison with the more sophisticated granular rheology having a shear-dependent friction coefficient $\mu(I_v)$ is also given in figures 6 and 7 (two-dimensional, black dashed line; and three-dimensional, black solid line for $h_f = 8$ mm). A best fit using the method of least squares provides good agreement with both experimental q_v and h_m for $\mu_1 = 0.24$, $\mu_2 = 0.39$, $I_0 = 0.01$ and $\eta_e/\eta_f = 6.6$. Note that the fitting gives the same friction coefficient of 0.24 for the Coulomb and granular rheologies but different effective viscosities. Using the fitted Coulomb and granular rheologies leads to similar predictions for the two- and three-dimensional cases. The predictions are

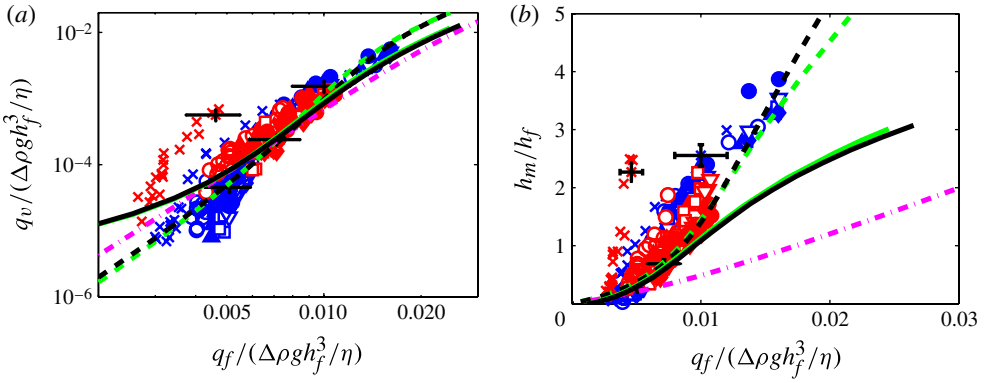

FIGURE 8. (Colour online) Same as figure 6 but for the scanned data across the channel: runs 5 (dark grey; blue online) and 15 (mid grey; red online) (symbols corresponding to the lateral position in table 2).

quite similar because the two- and three-dimensional models contain the same physical ingredient (the frictional rheology) and the fitting parameters are adjusted to match the experimental observations.

Three-dimensional effects have been examined more thoroughly in runs 5 and 15 detailed in table 2 for which the rectangular pipe is scanned to obtain a three-dimensional investigation of the flow field. Note that the two runs correspond to two different particle–fluid combinations. Figure 8 shows q_v and h_m versus the two-dimensional flow rate q_f using the geometrical coefficient k, which provides the switch from three- to two-dimensional fluid flow rate and depends on the location across the channel (see (2.1)). The same good collapse and good agreements with the predictions of the three-dimensional numerical simulations taken in the middle plane are found except for the data close to the channel side where the granular motion is faster than predicted. This is a signature of a three-dimensional flow.

Figure 9 presents the variation across the channel of h_f, q_v, h_m and k. The fluid–sediment interface is approximately flat across the pipe except close to the channel sidewalls, for which it becomes slightly lower, of the order of a particle size. The three-dimensional predictions provide a better agreement for the variation of q_v and h_m than the two-dimensional calculations (both using the granular rheology). The geometrical coefficients inferred from the predictions of the numerical simulations using the granular rheology and from (2.1) are in excellent agreement. This indicates that, in the present flow regime, the perturbation induced by the granular motion on the flow is weak and thus that the use of this coefficient is valid. Note that the flow corresponding to run 5 ($h_f = 8.1$ mm) presents a much wider flat range of k than that corresponding to run 15 ($h_f = 16.3$ mm). Figure 10 shows that the fluid velocity profiles are well described by both the three- and two-dimensional calculations using the granular rheology. Inside the mobile sediment the three-dimensional predictions again provide a better agreement for the velocity profile, in particular close to the sidewalls, where the experiments show that the granular motion is faster than the two-dimensional predictions.

Finally, we provide two-dimensional comparison with the two-phase modelling using the more complex constitutive law recently proposed by Boyer *et al.* (2011) in figures 11 and 12. This new rheology, for which none of the parameters has been

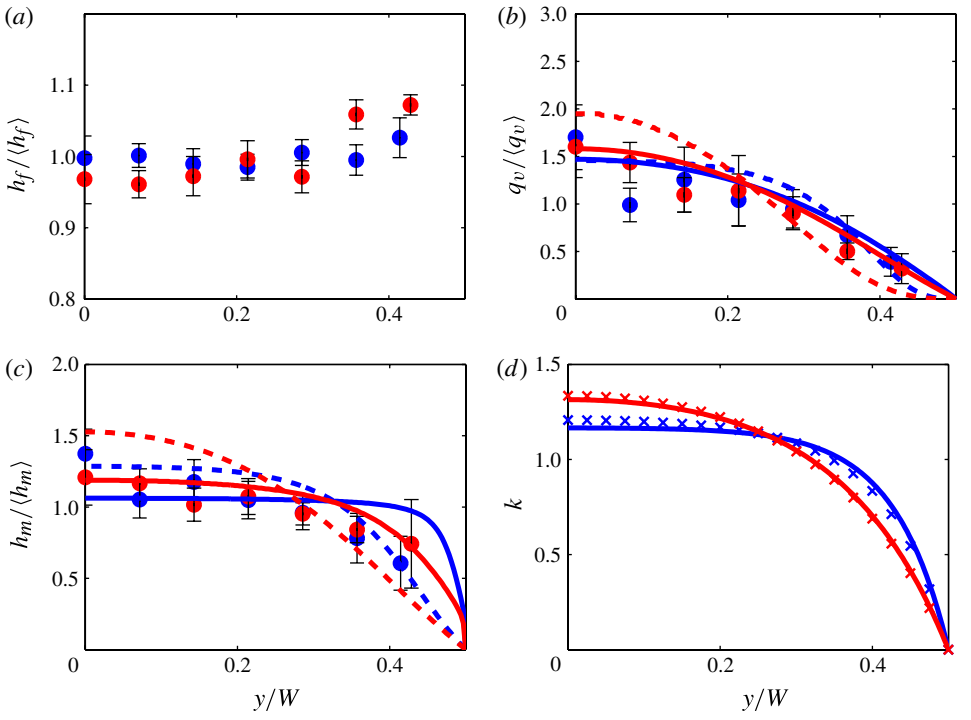

FIGURE 9. (Colour online) Variation across the channel of the averaged scanned measurements for runs 5 (dark grey (blue online), $h_f \subset [8\text{–}10]$ mm) and 15 (mid grey (red online), $h_f \subset [15\text{–}18]$ mm) detailed in table 2. (*a*) Averaged fluid thickness normalized by the mean fluid thickness across the channel. (*b*) Averaged particle velocity flux q_v normalized by the mean particle velocity flux. (*c*) Averaged thickness of the mobile layer h_m normalized by the mean thickness of the mobile layer. (*d*) Geometrical coefficient k obtained in the 3D numerical simulations using the granular rheology corresponding to run 5 conditions ($\times$ (dark grey; blue online), $h_f = 8.1$ mm) and to run 15 conditions ($\times$ (mid grey; red online), $h_f = 16.3$ mm) and using (2.1) for $h_f = 8.1$ mm (dark grey solid line; blue online) and $h_f = 16.3$ mm (mid grey solid line; red online). Comparison with the two-phase model using the granular rheology with $\mu_1 = 0.24$, $\mu_2 = 0.39$, $I_0 = 0.01$ and $\eta_e/\eta_f = 6.6$ (2D, dashed line; and 3D, solid line, for $h_f = 8.1$ mm (dark grey; blue online) and $h_f = 16.3$ mm (mid grey; red online)) is provided in panels (*b*) and (*c*).

adjusted, gives a good order of magnitude. However, the predicted velocity profile is much stiffer and this yields an underestimation of q_p, q_v and h_m. In figure 12, we have also given the variation of ϕ along z. Good agreement is found between the model and the experiments. The volume fraction ϕ is nearly constant along z except on typically two particle diameters at the top where it rapidly goes to zero. This gives grounds for having a constant particle volume fraction in the previous Coulomb and granular models.

5. Discussion and conclusion

We have investigated the mobile layer of a granular bed composed of spherical particles in a laminar rectangular channel flow. We have measured both particle and fluid velocities using particle image velocimetry for different index-matched

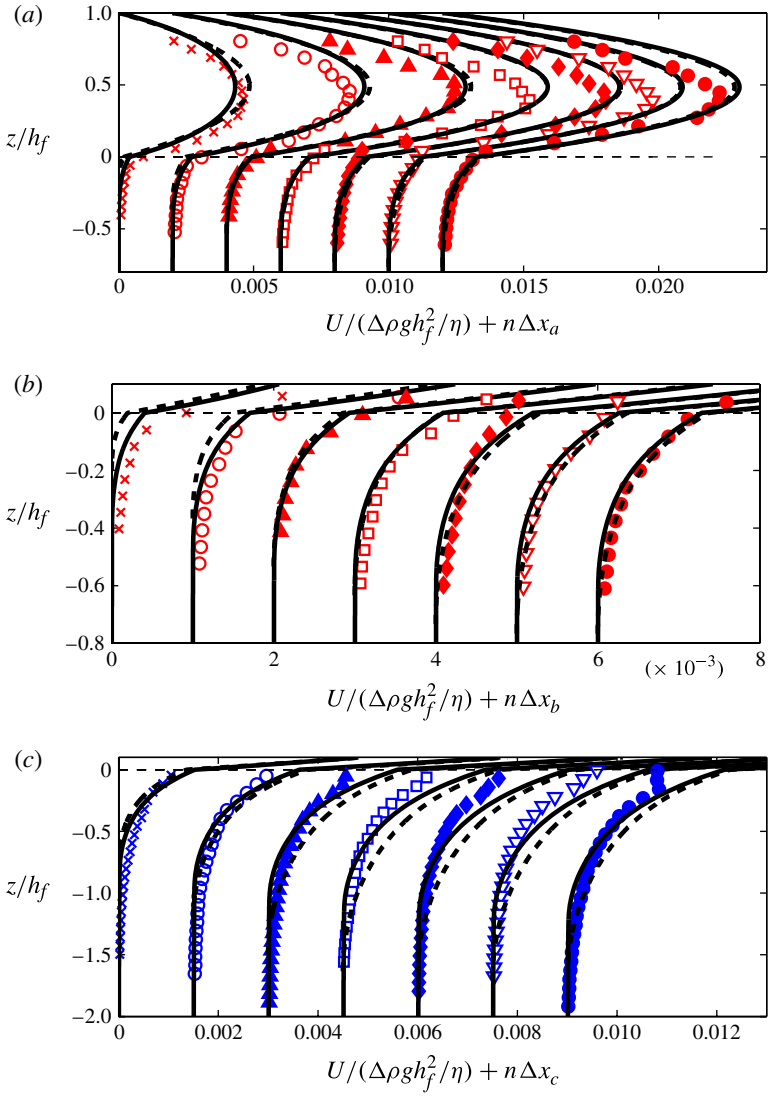

FIGURE 10. (Colour online) Comparison of the dimensionless velocity profiles between experiments corresponding to the different locations of (*a*,*b*) run 15 for $h_f = 16.7$ mm and (*c*) run 5 for $h_f = 8.1$ mm (symbols in table 2) and theoretical two-phase model using the granular rheology (2D, black dashed line; and 3D, black solid line). The plots are shifted for clarity ($\Delta x_a = 0.002$, $\Delta x_b = 0.001$, $\Delta x_c = 0.0015$). Panel (*b*) is a blow-up of panel (*a*).

combinations of particles and fluid and for a wide range of fluid flow rates above incipient motion. An analysis of the velocity and concentration profiles inside the mobile granular layer shows that: (i) there is no significant velocity slip between the particles and the fluid; and (ii) the particle volume fraction is approximately constant except at the bed interface where it vanishes on typically two particle diameters. An investigation of the appropriate scalings shows that adopting the fluid height as the length scale and a viscous time scale as suggested by a continuum modelling using a frictional rheology for the particulate phase gives a good collapse of the data for the particle flux, thickness of the mobile layer and velocity profiles.

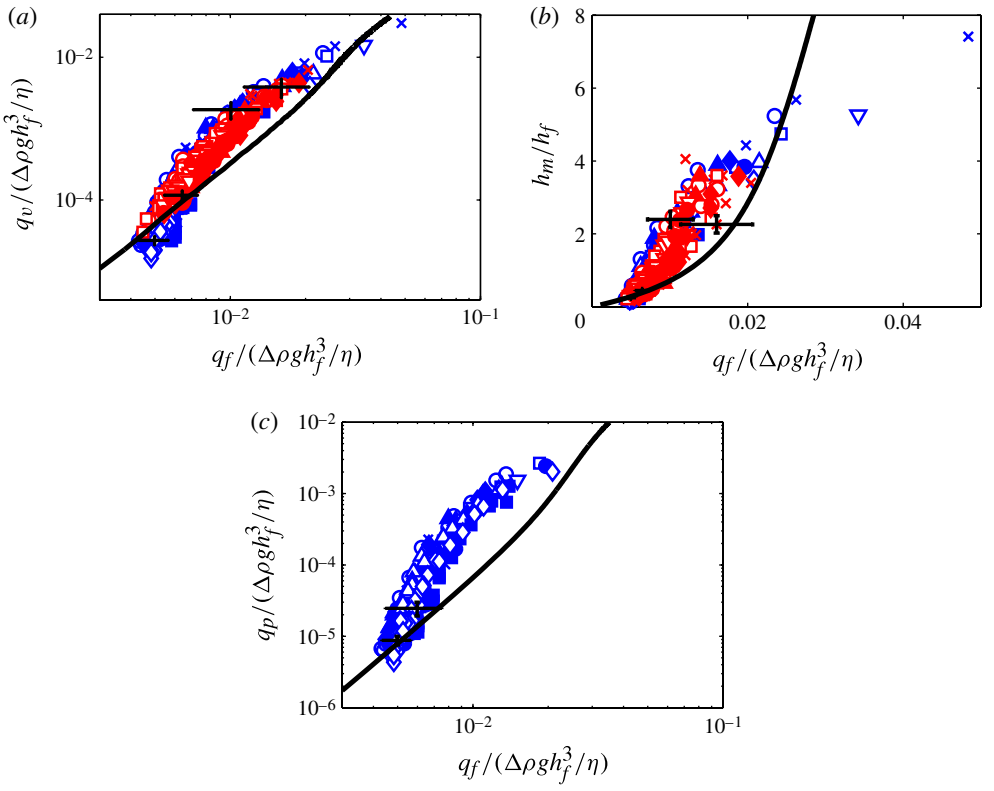

FIGURE 11. (Colour online) (*a*,*b*) Same as figure 6 and (*c*) particle flux $q_p/(\Delta\rho g h_f^3/\eta)$ with comparison to the two-phase model using the suspension rheology of Boyer *et al.* (2011) (2D, solid line).

The measurements are then compared to a two-phase continuum approach having a frictional rheology for the particle phase and a Newtonian rheology for the fluid phase originally proposed by Ouriemi *et al.* (2009). The simplest constitutive model using a realistic Coulomb friction coefficient of 0.32 and an Einstein viscosity and assuming uniform particle concentration inside the mobile layer yields realistic particle flux but fails to predict the bedload thickness as well as the velocity profiles. Good agreement is obtained by fitting the two parameters of this rheology, i.e. the friction coefficient and the effective viscosity. The obtained value for the friction coefficient is 0.24 and is smaller than that found in rheological measurements (Boyer *et al.* 2011), while the value for the effective viscosity is 14 and is much larger than that used in the porous media literature (see e.g. Goharzadeh *et al.* 2005). This large viscosity is able to describe the slope of the velocity profile at the interface but is not realistic. This inconsistency can be overcome by using a shear-dependent friction rheology (having the same static friction coefficient of 0.24), which provides excellent agreement with a lower effective viscosity of 6.6. Note that we recover a viscosity of the order of magnitude of that of the Einstein viscosity as in a porous medium (see the discussion of § 3.2(i)). In addition, this rheology implemented in a full three-dimensional simulation is able to describe three-dimensional effects observed at larger flow rates as well as the flow variation across the channel. The two friction

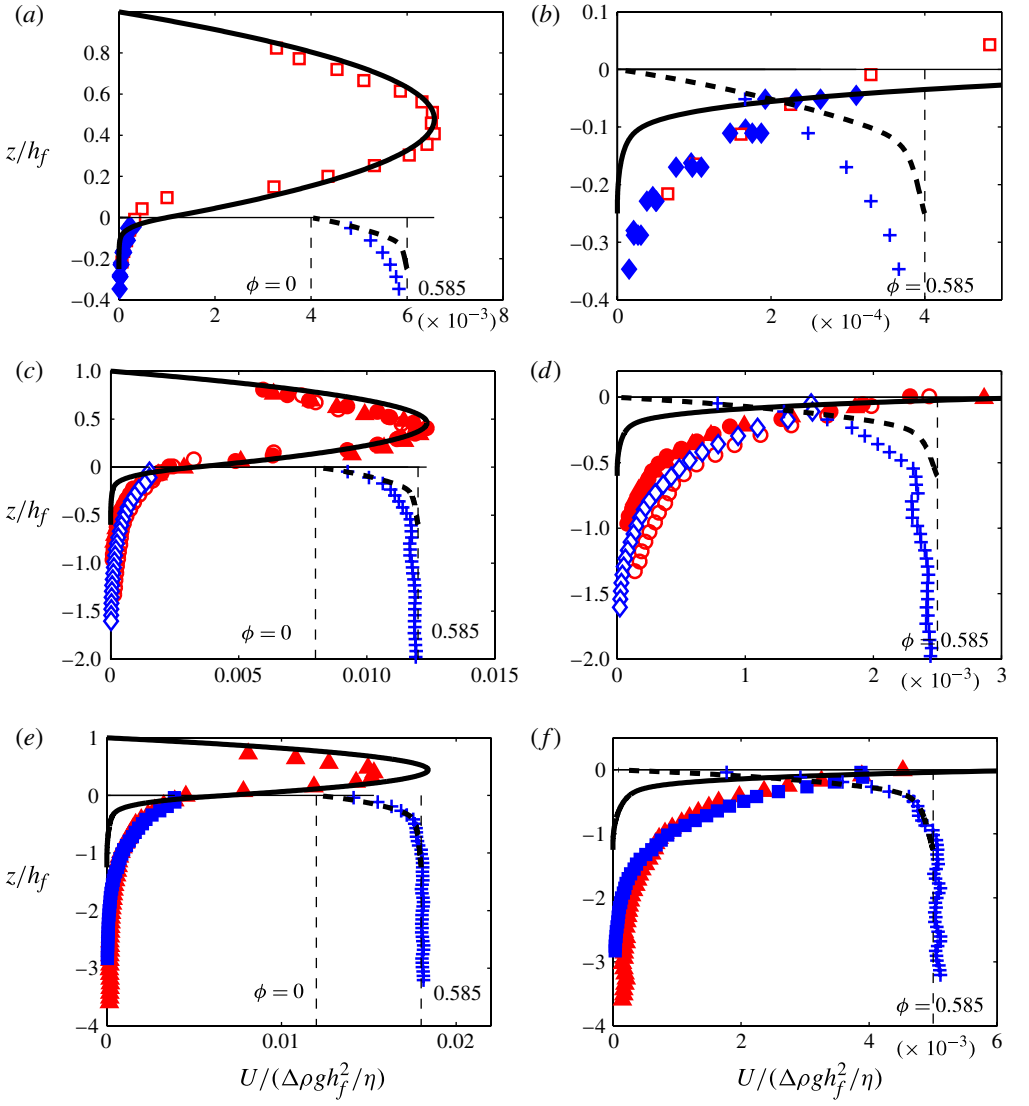

FIGURE 12. (Colour online) Same as figure 7 but with comparison to the two-phase model using the suspension rheology of Boyer *et al.* (2011) (2D, solid line). The variation of ϕ along z is also represented (+, dark grey (blue online), experiments; and black dashed line, 2D predictions).

coefficients μ_1 and μ_2 in the $\mu(I)$ rheology are slightly lower than those expected. This may be due to additional phenomena such as dilatancy, which, though small, could act to reduce friction in the present experimental configuration (see e.g. Pailha & Pouliquen 2009). The more complex rheological model proposed by Boyer *et al.* (2011) having no adjustable parameters gives the proper trend and good order of magnitude but fails to describe the velocity profile. This third model comes from rheological measurements of dense suspensions of neutrally buoyant spheres using pressure-imposed rheometry and may not be directly applicable to buoyant suspensions with a strong gradient of concentration at the particle–fluid interface. Again, the dilatancy effect should also be included in this model.

To conclude, a two-phase continuum model having a frictional rheology for the particle phase is able to predict quantitatively the flow inside the mobile layer of a sheared granular media. Three rheological constitutive laws having increasing degrees of sophistication have been tested and discussed. Clearly, among these three rheological models, the granular model is the most successful, but the simplest analytical Coulomb model still gives a sensible prediction for the particle flux. It would be good to have in the future a robust rheological model employed to predict the behaviour of a wide class of dense particulate flows. The present experimental data can be used as a benchmark for rheological models in a continuum approach but also for a particle interaction model in discrete-particle simulations.

Acknowledgement

Funding from Agence Nationale de la Recherche (Project Dunes ANR-07-3 18-3892) is gratefully acknowledged.

Supplementary movies

Supplementary movies are available at http://dx.doi.org/10.1017/jfm.2013.546.

REFERENCES

ANDREOTTI, B., FORTERRE, Y. & POULIQUEN, O. 2013 *Granular Media: Between Fluid and Solid*. Cambridge University Press.

BAGNOLD, R. A. 1954 Experiments on a gravity-free dispersion of large solid spheres in a Newtonian fluid under shear. *Proc. R. Soc.* A **225**, 49–63.

BAGNOLD, R. A. 1956 The flow of cohesionless grains in fluids. *Phil. Trans. R. Soc.* A **249**, 235–297.

BOYER, F., GUAZZELLI, É. & POULIQUEN, O. 2011 Unifying suspension and granular rheology. *Phys. Rev. Lett.* **107**, 188301.

BRINKMAN, H. C. 1947 A calculation of the viscous force exerted by a flowing fluid on a dense swarm of particles. *Appl. Sci. Res.* A **1**, 27–34.

CASSAR, C., NICOLAS, M. & POULIQUEN, O. 2005 Submarine granular flows down inclined planes. *Phys. Fluids* **17**, 103301.

CHAUCHAT, J. & MÉDALE, M. 2010 A three-dimensional numerical model for incompressible two-phase flow of a granular bed submitted to a laminar shearing flow. *Comput. Meth. Appl. Mech. Engng* **199**, 439–449.

CHAUCHAT, J. & MÉDALE, M. 2014 A three-dimensional model for dense granular flows based on the $\mu(I)$ rheology. *J. Comput. Phys.* **256**, 696–712.

CHARRU, F., MOUILLERON-ARNOULD, H. & EIFF, O. 2004 Erosion and deposition of particles on a bed sheared by a viscous flow. *J. Fluid Mech.* **519**, 55–80.

DERKSEN, J. 2011 Simulations of granular bed erosion due to laminar shear flow near the critical Shields number. *Phys. Fluids* **23**, 113303.

DIJKSMAN, J. A., RIETZ, F., LÕRINCZ, K. A., VAN HECKE, M. & LOSERT, W. 2012 Refractive index matched scanning of dense granular materials. *Rev. Sci. Instrum.* **83**, 011301.

FORTERRE, Y. & POULIQUEN, O. 2008 Flows of dense granular media. *Annu. Rev. Fluid Mech.* **40**, 1–24.

GOHARZADEH, A., KHALILI, A. & JØRGENSEN, B. B. 2005 Transition layer thickness at a fluid–porous interface. *Phys. Fluids* **17**, 057102.

JACKSON, R. 1997 Locally averaged equations of motion for a mixture of identical spherical particles and a Newtonian fluid. *Chem. Engng Sci.* **52**, 2457–2469.

JACKSON, R. 2000 *The Dynamics of Fluidized Particles*. Cambridge University Press.

LAJEUNESSE, E., MALVERTI, L., LANCIEN, P., ARMSTRONG, L., METIVIER, F., COLEMAN, S., SMITH, C. E., DAVIES, T., CANTELLI, A. & PARKER, G. 2010 Fluvial and submarine morphodynamics of laminar and near-laminar flows: a synthesis. *Sedimentology* **57**, 1–26.

LOBKOVSKY, A. E., ORPE, A. V., MOLLOY, R., KUDROLLI, A. & ROTHMAN, D. H. 2008 Erosion of a granular bed driven by laminar fluid flow. *J. Fluid Mech.* **605**, 47–58.

LOISELEUX, T., GONDRET, P., RABAUD, M. & DOPPLER, D. 2005 Onset of erosion and avalanches for an inclined granular bed sheared by a continuous laminar flow. *Phys. Fluids* **17**, 103304.

MALVERTI, L., LAJEUNESSE, E. & MÉTIVIER, F. 2008 Small is beautiful: upscaling from microscale laminar to natural turbulent rivers. *J. Geophys. Res.* **113**, F04004.

MEUNIER, P. & LEWEKE, T. 2003 Analysis and minimization of errors due to high gradients in particle image velocimetry. *Exp. Fluids* **35**, 408–421.

MOUILLERON, H., CHARRU, F. & EIFF, O. 2009 Inside the moving layer of a sheared granular bed. *J. Fluid Mech.* **628**, 229–239.

NICOLAS, X., LUIJKX, J.-M. & PLATTEN, J.-K. 2000 Linear stability of mixed convection flows in horizontal rectangular channels of finite transversal extension heated from below. *Intl J. Heat Mass Transfer* **43**, 589–610.

OURIEMI, M., AUSSILLOUS, P. & GUAZZELLI, É. 2009 Sediment dynamics. Part 1. Bed-load transport by laminar shearing flows. *J. Fluid Mech.* **636**, 295–319.

OURIEMI, M., AUSSILLOUS, P., MÉDALE, M., PEYSSON, Y. & GUAZZELLI, É. 2007 Determination of the critical Shields number for particle erosion in laminar flow. *Phys. Fluids* **19**, 061706.

PAILHA, M. & POULIQUEN, O. 2009 A two-phase flow description of the initiation of underwater granular avalanches. *J. Fluid Mech.* **633**, 115–135.

VAN DER HOEF, M. A., BEETSTRA, R. & KUIPERS, J. A. M. 2005 Lattice–Boltzmann simulations of low-Reynolds-number flow past mono- and bidisperse arrays of spheres: results for the permeability and drag force. *J. Fluid Mech.* **528**, 233–254.

VAN RIJN, L. C. 1984 Sediment transport, Part I: bed load transport. *J. Hydraul. Engng* **110**, 1431–1456.